High-efficiency anti-reflective modification of freeform elements and cylindrical lenses for arrayed wide-field astronomical corrector units

Uma Subash[a,*] Hanshin Lee[b] and Menelaos K. Poutous[a]

[a]University of North Carolina at Charlotte, Department of Physics and Optical Science, Charlotte, North Carolina, United States

[b]University of Texas – Austin, McDonald Observatory, Austin, Texas, United States

ABSTRACT. Randomly distributed anti-reflective nanostructures were fabricated on both surfaces of cylindrical lenses and freeform optical elements using a plasma-assisted reactive-ion etching technique. An average spectral transmission of 98% was measured across the wavelength range from 340 to 800 nm. Mid-band full-angle directional scatter measurements show a difference of six orders of magnitude in transmission intensity between specular and off-specular angles. Measurements before and after the etching process show little to no wavefront distortion for the cylindrical lenses. The enhanced transmission optics were used as part of the dual-unit arrayed wide-field astronomical camera system tested on the Harlan J. Smith telescope at the McDonald Observatory, and their performance was contrasted with conventional thin film coated component performance.

1 Introduction

Although challenging in design and fabrication, broadband anti-reflection (BBAR) coatings are of significant importance considering photon flux performance improvements in optical instruments like telescopes, or devices, such as power sensors, solar cells, and imaging detectors. Conventional anti-reflection optical surface treatments include single-film quarter-wave coatings for single layer antireflection (SLAR) and multi-layer anti reflection (MLAR) for wider bands.[1,2] For SLAR, the major challenge is the availability of materials that match the optical interface impedance for the substrate of choice. Thin films with gradient index profiles can facilitate impedance matching more easily and enable effective anti-reflectivity over wider angles of incidence and broader wavelength bands.[3–5] Balanced compromise solutions, between fabrication complexity and desirable performance, are often implemented. Vapor deposition, electrostatic layer-to-layer deposition, and sputtering are some conventional thin film fabrication techniques used.[6–8] The inevitability that materials with thermal and mechanical mismatched properties are deposited on the substrate can be of concern for some instruments or applications, especially if the optics are to function in environments with variable ambient conditions.

*Address all correspondence to Uma Subash, usubash@uncc.edu

In recent years, random anti-reflective subwavelength surface structures (rARSS) have been introduced as substitutes for traditional thin film coatings. These structures have demonstrated excellent performance as anti-reflective surfaces across various spectral ranges, including the visible, short-wave, and mid-wave infrared regions.[9–12] Furthermore, their monolithic fabrication into the substrate surface, primarily through reactive ion plasma etching processes, endows them with higher thermal stability and mechanical durability.[13] Unlike conventional thin film coatings, rARSS do not necessitate complex design efforts, since their random nature makes the optimization of fabrication parameters the primary design objective. While most of the research on rARSS has focused on planar substrates and interfaces, achieving transmission rates exceeding 99% on fused silica (FS) substrates,[14] there have also been a few documented studies on the optical performance of rARSS on non-planar surfaces, such as lenses.[15–18]

In astronomy, these aspects render the rARSS an attractive broadband alternative to thin film AR coatings for imaging and spectroscopic systems with multiple air-glass interfaces. One example is the arrayed wide-angle camera system (AWACS).[19,20] Unlike the traditional wide-field corrector design based on multiple large lenses or mirrors, the AWACS accomplishes desired field expansion via a suite of small cost-effective electro-opto-mechanical units over a telescope's focal surface, for local and simultaneous telescope field aberration and atmospheric dispersion compensation (ADC). All units share one common electro-opto-mechanical design, featuring imaging lenses for the underlying optical relay, a combination of an adaptive cylinder lens pair and simple freeform lens for field aberration correction, and a miniature prism pair as an ADC element. The design commonality in AWACS allows leverage of significant cost and complexity scaling while transitioning from a $2 \sim 3$ m class telescope to 30 m-class Extremely Large Telescope and beyond. Due to the large (22×) number of air-glass interfaces in each AWACS unit, it is critical to minimize the loss from Fresnel reflection and scattering over a broad wavelength range from 365 to 1000 nm. The rARSS exhibits characteristics that are ideal to meet such a need.[21–23]

To the best of our knowledge, research to date has primarily focused on assessing the optical transmission performance of random structures including some comparisons between lenses with thin film anti reflection (TFAR) and rARSS,[15,16,18] without investigating optical system-level effects. Potential scattering or wavefront distortions caused by the presence of rARSS-enhanced components in an optical system are not available in the existing literature. The topography of non-planar surfaces may lead to significant alterations of the rARSS average density and local profiles, since their fabrication consists of a top-down high-power reactive etching process. The present report examines the impact of rARSS on the performance of the freeform elements and cylindrical lenses as used in the AWACS system, as individual elements and at the system level, specifically evaluating their spectral transmission, scattering effects, and wavefront distortion. We conducted measurements of the cylindrical wavefronts emerging through the lenses and the bidirectional scatter distribution function of the freeform element, both before and after applying rARSS. The enhanced elements were placed in an arrayed wide-field astronomical camera system unit assembly, and comparative field tests were performed with the Harlan J. Smith telescope (HJST) at the McDonald Observatory.

2 Fabrication and Test Methods

There are two steps in rARSS fabrication on optical surfaces: the deposition of a porous masking layer and, etching the unmasked nanopores into columnar nanostructures directly into the substrate. Our approach was to use a DC-magnetron sputtering tool (AJA International ATC 1800-F) to deposit a thin porous layer of gold (<40 nm) on the component surfaces, serving as the partial mask for the randomly distributed feature etch. The sputtering process control parameters (time, magnetron power) were optimized based on prior process development steps.[24] We employed an anisotropic reactive-ion plasma etch step (PlasmaTherm RIE7000) to permanently transfer the nanopore random profile into the light entry and exit surfaces of the cylindrical lenses and freeform components. In our process, the 600-W RF-driven reactive plasma contains sulfur-hexafluoride (SF_6). The etching parameters were optimized to achieve the required broadband transmission enhancement in the visible spectral region between 340 and 800 nm, with the Fresnel transmission at 633 nm enhanced to 99.5% per surface, based on planar FS witness sample measurements.

Three different optical component sets were used: a plano-concave cylindrical lens set (PCV), a plano-convex cylindrical lens set (PCX), and an optical freeform-surface set (FF). All components were made with Corning Fused Silica 7980. The cylindrical lenses are 11 mm in diameter, with a radius of curvature of 400 mm on the curved side, yielding an effective focal length of +88.8 cm and −88.8 cm for the PCX and PCV sets respectively at 633 nm wavelength. The freeform component has an aperture diameter of 36 mm, and a wavefront surface described as

$$\text{Sag}(x, y) = -3.47\, Z_3(x, y; R) - 6.73\, Z_7(x, y; R), \tag{1}$$

where x, y are surface coordinates, and R is the normalization radius parameter, and the Zernike polynomials are

$$Z_3(x, y; R) = 2\left(\frac{y}{R}\right), \tag{2}$$

$$Z_7(x, y; R) = 2.83\left[3\left(\frac{x}{R}\right)^2 + 3\left(\frac{y}{R}\right)^2 - 2\right]\left(\frac{y}{R}\right). \tag{3}$$

The freeform total maximum sag across the clear aperture is 52 nm. The AR random structures were fabricated on both surfaces of all three sample sets. A total of six samples of each component set were made available for the study.

A grating spectrophotometer (Cary 60) was used to measure the directional optic axis transmission of all samples, before and after the rARSS etching process. The spectrophotometer uses an unpolarized broad-band light source (300 to 1900 nm) with a 1 mm beam spot diameter. The on-axis spectral transmission ratio, normalized to the incident intensity, was measured for each component from the three sets and then averaged within the set.

To examine potential wavefront distortion caused by the rARSS etching process, the wavefront of the samples was measured using the Shack-Hartmann (SH) wavefront sensor (ThorLabs WFS150-5C) before and after the process. The sensor is able to perform wavefront measurements within the 300 to 1100 nm peak-to-valley (PV) sag range. The prominent factors that affect the cylindrical lens profiles are the Zernike polynomials for astigmatism (Z_6) and defocus (Z_5), and the PV amplitude of the emerging cylindrical wavefront. The nomenclature of the Zernikes with just one parameter (Z_r) follows Malacara.[25] Additional Zernike polynomial terms,[26] such as tip and tilt, are reduced with alignment of the pieces under test. The sample was affixed to an axial rotational holder, positioned normal to the optic axis, allowing for adjustment of the azimuth angle. This arrangement ensured consistent alignment of all six samples of both types of cylindrical lenses. The SH source is a 50 mW, 650 nm wavelength diode laser, with a beam diameter of 4 mm. The baseline wavefront from the source is collimated and flattened by minimizing PV to 0.4 μm prior to individual sample measurements. The SH sensor exposure time was 0.27 s per capture, and 20 wavefronts were averaged per measurement. The pupil definition for the sensor was set to 5 mm in diameter to ensure full imaging of the beam. To account for possible light source fluctuations, data were collected for each sample before and after the rARSS process for a period of 3 to 5 days and averaged over the number of days for consistency. The freeform lens had a PV amplitude <0.4 μm range within the center field, and hence the profile was not discernible from a flat wavefront. We limited the wavefront measurements to the PCX and PCV cylindrical lenses.

To measure the redistribution of radiance on-axis and any possible induced off-axis scatter due to the presence of the rARSS structures, we measured the bi-directional transmission distribution function (BTDF) of a selected freeform sample. A complete equatorial-angle scatterometer instrument was used (CASI, Schmitt Industries Inc.). The instrument has a helium–neon laser source operating at 633 nm wavelength with a half-wave retarding plate and a linear polarizer to select the test polarization state. The instrument is capable of measuring scatter over the full 180 deg angular transmission range, as shown in Fig. 1. The sample under test was mounted on the linear translation stage perpendicular to the incident beam. The instrument signature (no sample baseline) and the sample BTDF are measured using a Si-detector with a separate linear polarizer (analyzer) that sweeps the path of the equatorial circle. The detector has auto-selecting multiple aperture diameters, performing a true radiometric detector measurement of irradiance,
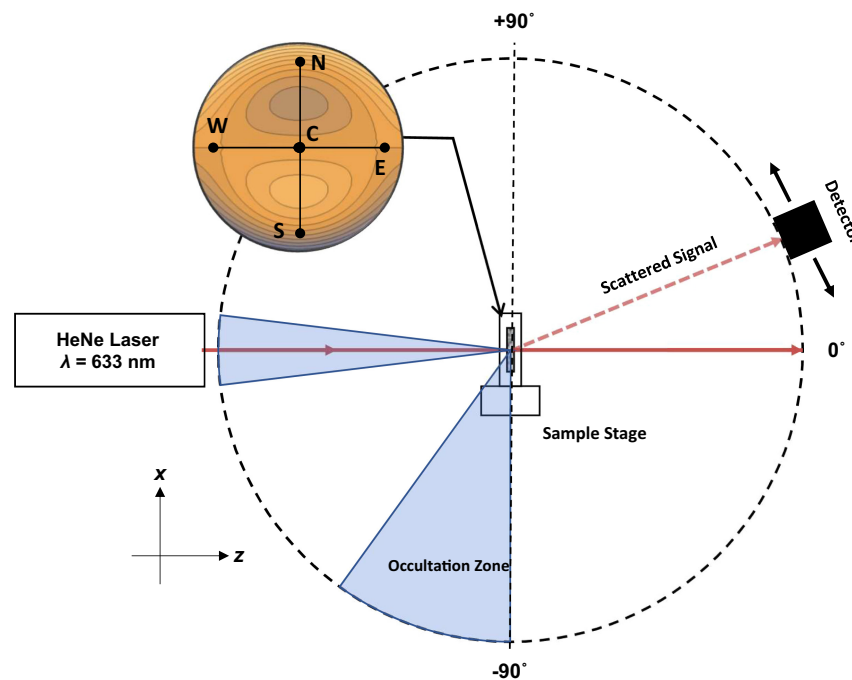
Fig. 1 Top-down view of the CASI scatterometer layout used to measure the scatter of the freeform element before and after etching. The BTDF is measured by sweeping the detector along the circular path from -90 deg to $+90$ deg. The inset shows the test locations on the freeform component surface facing the light source. The coordinate reference applies to the scatterometer.

which allows for a relative sensitivity range of nine-orders of magnitude. The freeform sample was mounted with the curved side facing the source, the sample stage was adjusted to allow for normal incidence, and the linear translator was used to select five test locations within the component. The test areas are labeled according to the inset orientation in Fig. 1.

3 Results

3.1 Component Transmission Enhancement
Figure 2 shows the measured normalized spectral axial transmission of the sample sets before and after rARSS processing for the PCV, PCX, and FF. The pre-process measurements were averaged over all six samples within each set of components. The maximum-minimum transmission range of measurements is shown as vertical bars. The resolution of the spectrometer was set to 1 nm. Following the double-sided rARSS etching process, the best four out of six measured samples were chosen from each set to be used in the corrector unit system. Table 1 lists the wavelength ranges where the transmission exceeds 98% for each set. The spectral transmission of the unprocessed samples averages to 93%, corresponding to an average 3.5% Fresnel reflectance per surface at normal incidence. The post-process transmission peaks at 99.1% for all sample types, indicating that the rARSS suppresses Fresnel reflectivity to a maximum of 0.5% per surface. The overall average transmission enhancement for the processed lens sets is 6% across the band of interest. The rARSS transmission curve is devoid of interference swings, compared to conventional thin film BBAR coatings. The bandwidth ($\Delta\lambda$) above 98% transmission is >400 nm for PCX and PCV lenses and >500 nm for the FF. The peak-efficiency band is 40 to 50 nm for the lenses and >100 nm for the FF.

3.2 Component Wavefront Measurements
As with any surface modification subtractive process such as reactive ion etching (RIE), there is concern that component sag or functionality could be altered. Since the cylindrical lenses and FF were etched to embed the rARSS on their surfaces, we considered wavefront tests for the PCX and PCV elements before and after processing. The lens-induced wavefront curvature depends on
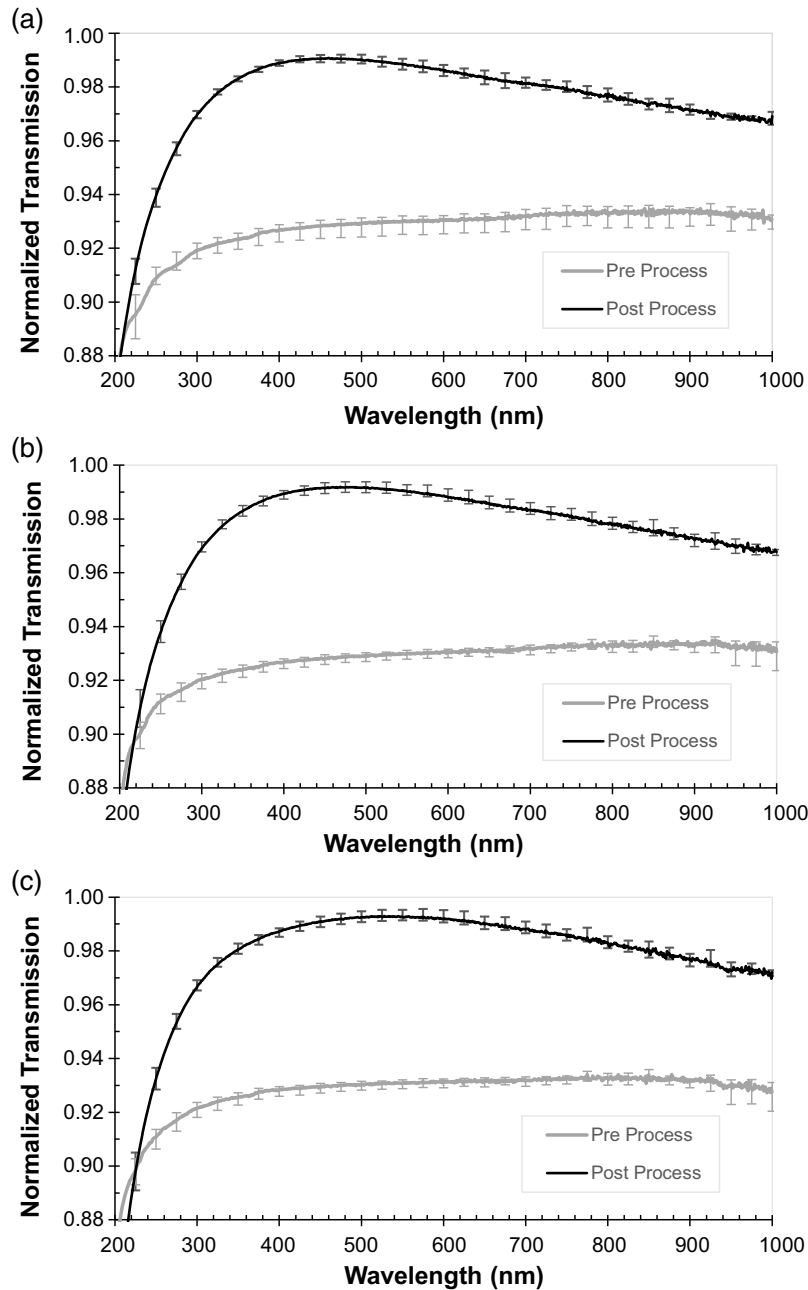
Fig. 2 Normal incidence axial transmission measurements, averaged across samples, for: (a) PCV lenses, (b) PCX lenses, and (c) the FF elements with 1 nm wavelength resolution. The pre-processed measurements are shown in gray and the rARSS double-sided enhanced measurements are in black. The bars indicate the within-set maximum to minimum range measurements for each wavelength, and are shown in 25 nm wavelength intervals.

the component surface sag and to distinguish between manufacturing and processing variations within the groups of lenses tested, we measured the cylindrical converging or diverging wavefront generated by each lens within a set.

The prominent factors that represent the cylindrical profile of the lenses are the wavefront PV-amplitude, Zernike coefficients Z_5 (defocus), and Z_6 (astigmatism). Table 2 shows global measurement averages calculated with the measured values from each lens over time and for each lens set. Figure 3 shows the fractional deviation (δ) of the time-averaged measurements

Table 1 Spectral normalized-transmission ranges, and peak transmission values with ranges, for the lens and FF sets from the measured test data shown in Fig. 2.

Sample	$\Delta\lambda$ for $T > 0.98$	T_{max}	$\Delta\lambda_{T_{max}}$
PCV	333 to 746 nm	0.991	438 to 484 nm
PCX	334 to 770 nm	0.992	466 to 503 nm
FF	347 to 851 nm	0.993	478 to 601 nm

Table 2 Across-sample measured global averages for PV, Z_5, and Z_6, pre- and post-rARSS processing, over all days of measurement. Values shown are in μm.

	$< pv >_t$		$< Z5 >_t$		$< Z6 >_t$	
Sample	Pre-processed	Post-processed	Pre-processed	Post-processed	Pre-processed	Post-processed
PCV	1.595	1.614	−0.379	−0.406	−0.631	−0.588
PCX	1.544	1.527	0.391	0.365	0.487	0.474

from the global average values listed in Table 2, and the design specifications where available. The fractional deviation is calculated using

$$\delta(x) = \frac{[< x >_t]_{\text{pre/post}}}{[< x >_{t,s}]_{\text{pre}}} - 1, \qquad (4)$$

where $< x >_t$ stands for either wavefront PV, Z_5, or Z_6 values, averaged across time measurements with index $t = 1,2,.5$; and $< x >_{t,s}$ is the global average, i.e., time-averaged measurements averaged across the number of samples per set ($s = 1,2,.6$).

Note that the $\delta(x)$ was calculated always using the global average pre-process to obtain the deviation post-process. The average wavefront PV fractional deviation before and after the rARSS process is within the specification range of $-0.03 < \delta(pv) < +0.03$, equivalent to an absolute wavefront $\lambda/10$ at 633 nm. The maximum range of wavefront PV fractional deviations within-sample measurements is caused by temporal environmental and alignment fluctuations in the testing conditions. The fractional deviations for Z_5 and Z_6 are within absolute wavefront deviations of $\lambda/8$ and $\lambda/10$, respectively.

Figure 4 shows the two-dimensional wavefront map with pixels along the x and y axes, for four tested cylindrical lenses. The 4 mm diameter beam spot spans approximately 20×20 pixels of the SH sensor. On the left column of the figure, the wavefront maps of the cylindrical components are displayed post-processing with rARSS, where the colorbars represent the wavefront concavity or convexity in micrometers. It is evident that the cylindrical profile is maintained for all four components after process with the first two being convex and the bottom two being concave. The maximum wavefront sag of all four components is nearly 1.6 μm, indicated by the yellow on the colorbar, corresponding to the previously mentioned wavefront PV amplitude, which is tabulated in Table 2. On the right column of Fig. 4, the residual wavefront is shown, calculated by subtracting the pre-processed wavefront map from the post-processed one pixel by pixel. The wavefront PV amplitude of these residuals is approximately 0.4 μm, within the baseline uncertainty (no sample) wavefront of the sensor, further suggesting minimal distortion in the wavefront. While only wavefront maps for 4 components are presented, all 12 components exhibited similar performances, and the maximum/minimum ranges are incorporated in the data of the wavefront PV amplitude graphs (Fig. 3).

3.3 Component Surface Scatter
The BTDF was measured following the procedure in Sec. 2. Any scattering effects prior-to and post-etching, are detectable within nine orders of magnitude in radiance across the equatorial
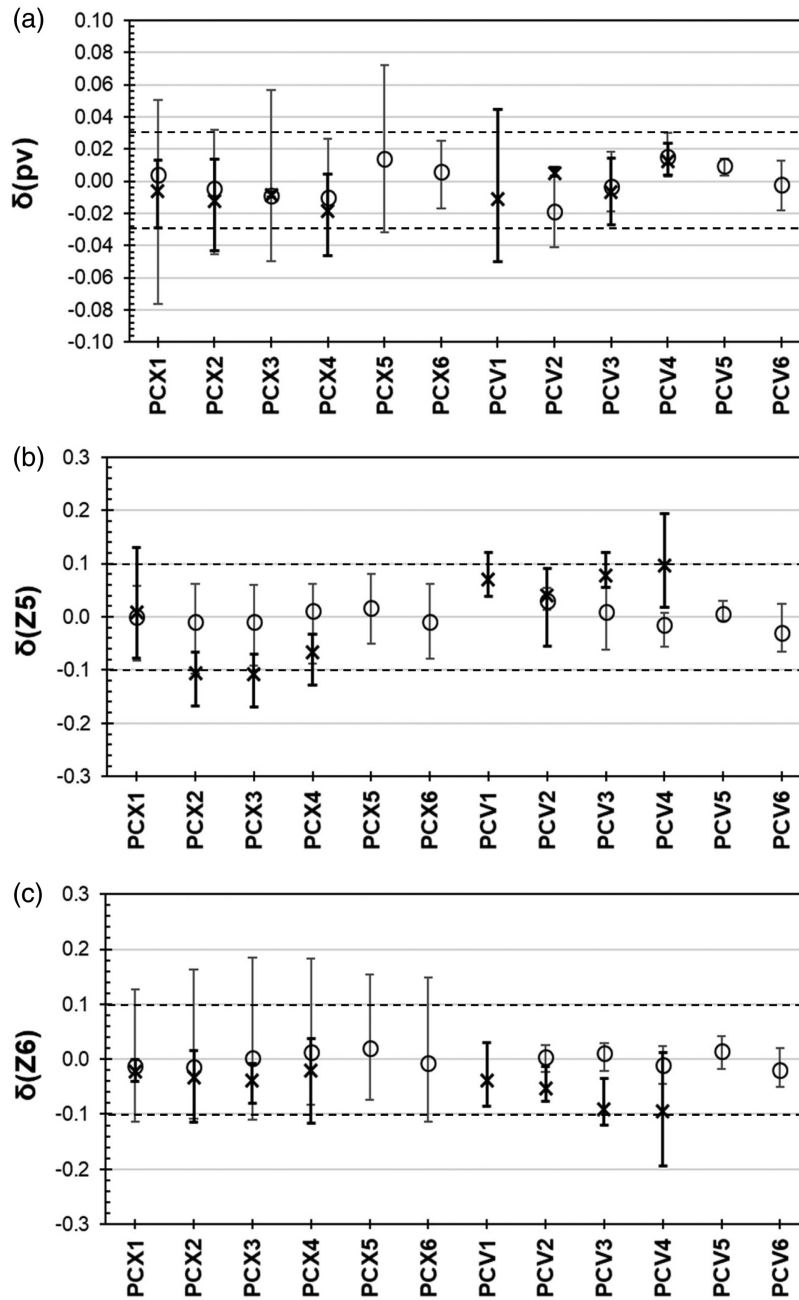
Fig. 3 Comparative wavefront measurements for all PCX and PCV cylindrical lenses, before (circles) and after (bold font crosses) rARSS enhancement. Fractional deviation of: (a) wavefront PV amplitude of the cylindrical profile, $\delta(pv)$; (b) defocus Zernike coefficient $\delta(Z5)$; and (c) astigmatism Zernike coefficient $\delta(Z6)$. The bars indicate the maximum deviation range of measurements across time (days). Thin bars belong to the pre-processing evaluation and thick bars to post-processing tests. The horizontal dashes indicate component specification limits.

optical xz-plane. Figure 5 shows the FF logarithmic-scaled BTDF, measured at the five cardinal locations of the component shown in Fig. 1, as a function of the angle of collection of the detector (θ_s) and the associated variable β_s. The collection-coordinate transformation: $\beta_s = \sin \theta_s$, plotted in a logarithmic scale, expands the axial beam profile measurements to separate finite-aperture diffraction effects from the axial radiance emerging from the tested component surfaces. The testing system signature beam profile, including the spatial-filtering aperture diffraction, is contained within $-3° < \theta_s < +3°$, shown in Fig. 5(b) as the vertical dotted line. Beyond this region the BTDF measured values are well below six orders of magnitude with respect to the
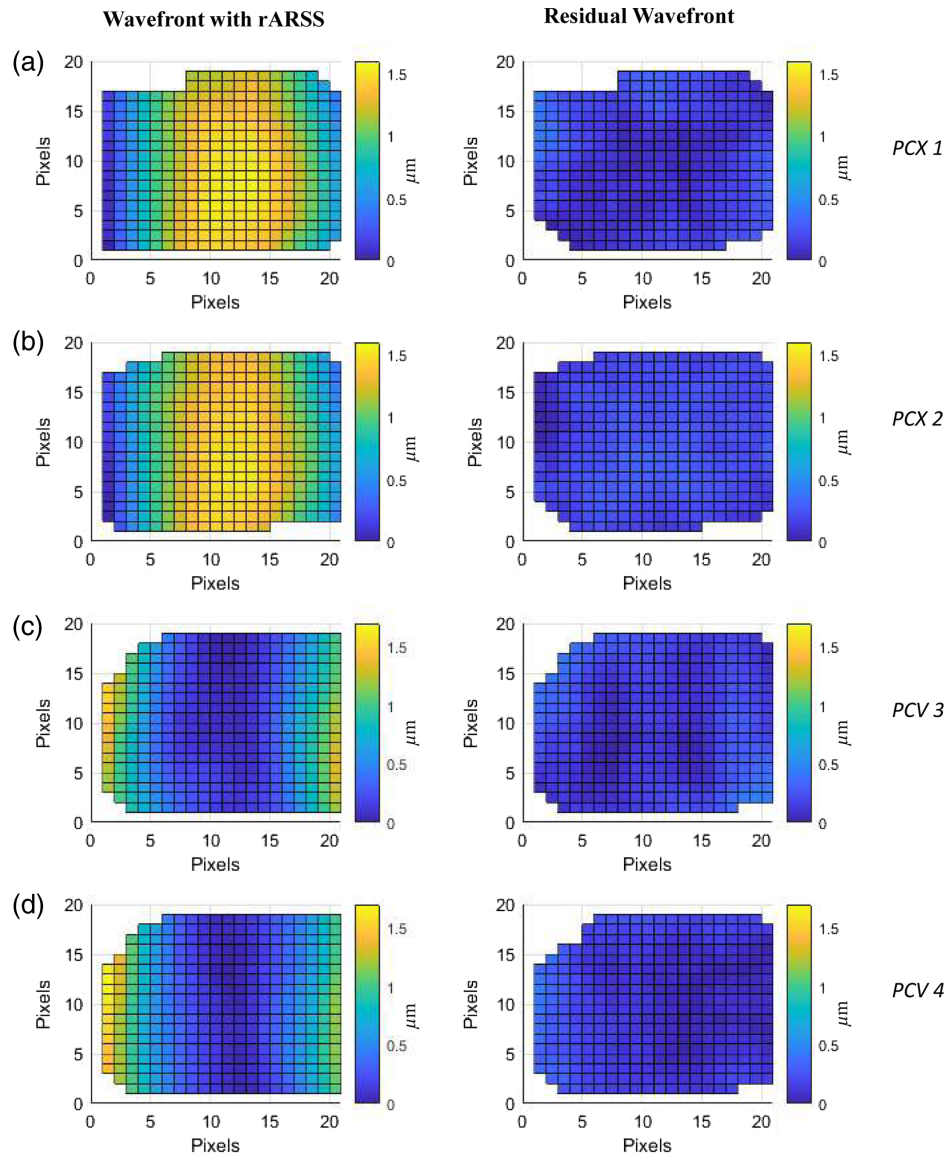
Wavefront with rARSS **Residual Wavefront**

Fig. 4 Pixel-to-pixel wavefront measurements of PCXs and PCVs post-process with rARSS shown on the left column, and the residual wavefront (pixel-to-pixel difference in wavefront of pre- and post-processed cylindrical components) shown on the right for four different lenses: (a) PCX1, (b) PCX2, (c) PCV3, and (d) PCV4. The color bar on each figure represents the convexity or concavity of the wavefront in μm from the base at 0 μm. The residual wavefront is within the baseline uncertainty (no sample) wavefront of the SH detector (0.4 μm sag).

peak value on-axis. The shoulder asymmetry of the N/E and S/W locations is due to the alignment and absolute polar orientation of the FF with respect to the detector orbit. These results indicate that the rARSS doesn't add excessive transmission scatter to the FF component.

Due to the low overall reflectivity (0.5%) and non-planarity of the FF component tested, we were not able to measure the bidirectional reflection distribution function (BRDF). To provide a quantitative comparison with the BTDF results shown in Fig. 5, we measured the BRDF of two optical-quality-flat FS windows with and without rARSS. Nano-structuring for both surfaces of the flat test-samples was achieved with the same RIE recipe used to modify the FF and cylindrical lenses in this study. Figure 6 shows the BRDF with respect to the reflection angle-of-collection associated variable β_c. The flats were tested at an angle-of-incidence (AOI) of -15 deg from the surface normal, and the specular reflected beam was located at $+15$ deg, corresponding to $\sin\beta_c = 0.26$. The BRDF wide-angle measurements are comparable with the corresponding BTDF values, indicating that there is bi-directional scatter due to the presence of the rARSS.
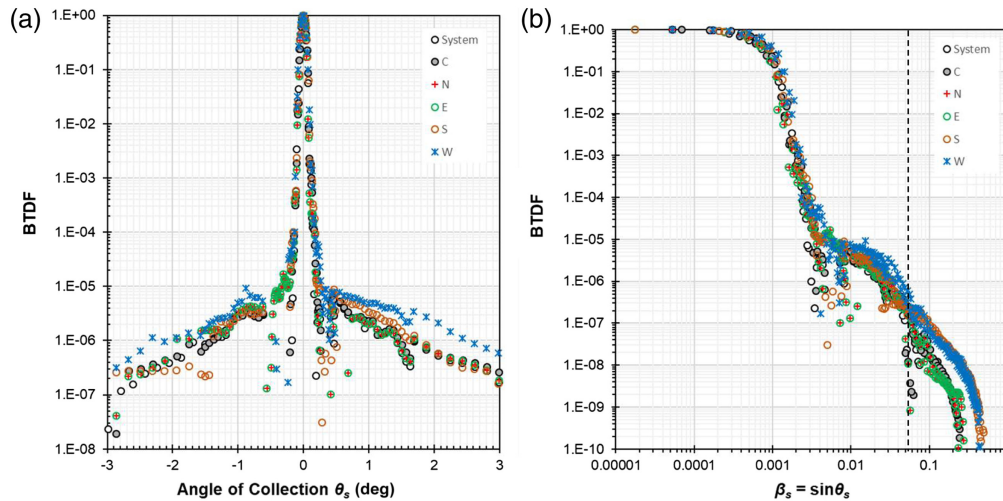
Fig. 5 BTDF measurements from the freeform element locations tested as shown in the inset of Fig. 1, compared with the instrument's signature. The BTDF scale is logarithmic. (a) BTDF measurements displayed as a function of the angle of collection (θ_s). (b) BTDF measurements displayed as a logarithmic function of the angular parameter β_s to accentuate comparisons in the axial direction. The vertical dotted line indicates the angular extent of the instrument's test beam.
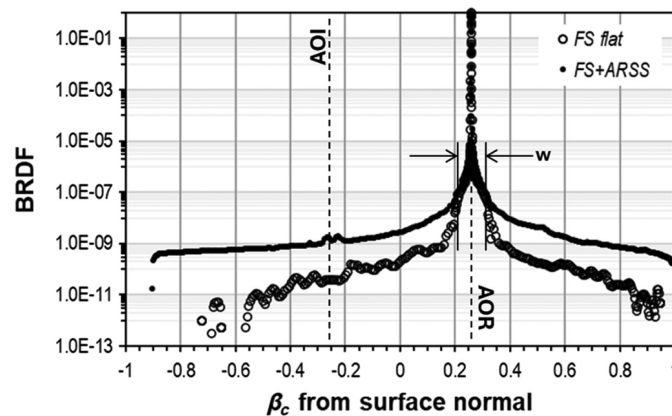

Fig. 6 BRDF measurements from an FS flat, compared with an FS flat with added ARSS on both surfaces (FS + ARSS). The BRDF measurements were taken at −15 deg angle-of-incidence (AOI) and are displayed as a logarithmic function of the angular parameter β_c with respect to the surface normal. The incident beam has a full angular width of 6 deg (w).

We note that the reflective near-axis scatter due to the presence of the nanostructures on the flat surface is on the order of 10^{-8}, an average of an order of magnitude lower than the BTDF. The BRDF of the rARSS-flat is higher than the polished silica flat surface for reflection collection angles wider than $\text{AOR} \pm 3^{\circ}$, symmetrically about the specular reflection.

4 System-level Performance Evaluation of the rARSS

To examine the throughput consistency between two units and to compare the throughput contributions from groups of optical elements with different AR treatments, the spectral transmission of two units has been measured. Each unit contains 1× free-form lens, 1× pair of cylinder lenses, 3× relay doublet pairs, and 1× ADC prism pair. The air-glass interfaces of the relay doublets and ADC prisms are coated with conventional MLAR-BBAR coatings while those of the cylindrical lens pair have been rARSS-modified as discussed earlier.

The 1:1 relay nature of the units allows us to evaluate this end-to-end throughput. Our in-house scanning spectrometer was used for this measurement. It consists of a fiber-fed broadband

light source at the focus of a collimator doublet on one side and a Silicon photo-diode (Newport 918D-UV) at the focus of a camera doublet on the opposite side. We used a laser-driven light source (LDLS EQ-99X-FC from Hamamatsu) filtered at a specific wavelength selected through a monochromator (Oriel Cornerstone 130 1/8m). The baseline spectral flux was measured with nothing between the doublets. The collimated beam diameter was 12 mm. Each relay unit was then mounted and aligned between the doublets. Note that the free-form lens is designed to be mounted separately from the unit optomechanics but the collimation space within the scanning spectrometer was too tight for it to be included. Hence, we excluded the free-form lens from the measurements. The measured spectral flux through each unit was normalized by the baseline to determine transmission.

The spectral transmission of each unit, along with the model prediction, is shown in the left panel of Fig. 7. This comparison is to evaluate the overall throughput deficit against the model prediction and consistency between the units. We note that the model prediction is based on the transmission analysis of the AWACS unit design within the Zemax Optics Studio and includes the published bulk transmission data from Ohara and Schott for all glass materials used as well as the vendor-supplied MLAR-BBAR measurements and our rARSS witness data.

Firstly, the units show nearly identical transmission, indicating consistency in the anti-reflective treatments applied to the optical components of the units. With respect to the model expectation, however, both units are less efficient. In particular, the blue part of the spectrum between 370 and 450 nm has a considerably large throughput deficit, even though we took great care to ensure high throughput in that spectral region by carefully specifying transmission requirements for the optical materials, surface finish, and AR treatments. To better understand this, we conducted additional measurements as follows. The mechanical design of the AWACS unit allowed measurement of the transmission with and without both the cylindrical lens pair and the ADC prism pair, which resulted in separating the throughput contributions between the relay lens system, the ADC prism pair, and the cylinder lens pair.

Using these data, we were able to estimate the performance of AR treatments applied to these portions, which is shown on the right panel of Fig. 7. The "relay per surface (TFAR)" curve has been reduced first by dividing out the bulk transmission of the corresponding relay-lens-only unit model, again based on the published data, from its spectral measurement. This leaves the contributions (T_{relay}) other than the bulk-transmission. It is reasonable to assume that T_{relay} is dominated by the AR treatment as the manufacturing data of all optical components
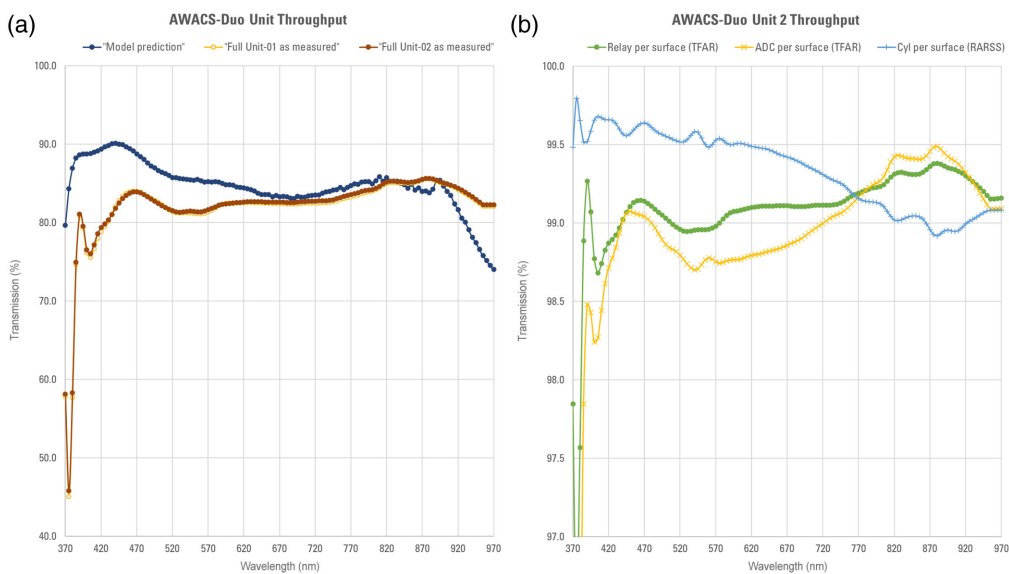

Fig. 7 (a) End-to-end spectral transmission measurements of AWACS-Duo units: U1 (yellow line and bullets) and U2 (brown line and bullets), including the model prediction (blue line and bullets). The results for U1 and U2 are overlapping. (b) Per-surface transmission estimate of different anti-reflective treatments applied to U2 components, based on spectral transmission measurements from component substitutions discussed in the text.

suggested exceeding the surface finish requirement. We then take the N'th root of T_{relay}, where $N = 12$ surfaces for the relay-only unit, to estimate the per-surface transmission. For the "ADC per surface (TFAR)" curve, we first derive $T_{\text{relay+ADC}}$, which contains the AR contributions from both ADCs and relay doublets but without the bulk transmission and then take the N'th root of $T_{\text{relay+ADC}}/T_{\text{relay}}$ where $N = 4$. Finally, for the "Cyl per surface (RARSS)" curve, we derive $T_{\text{relay+ADC+Cyl}}$ which contains the AR contributions from ADCs, cylinder lenses, and relay doublets but without the bulk transmission and then take the N'th root of $T_{\text{relay+ADC+Cyl}}/T_{\text{relay+ADC}}$ where $N = 4$. We note that the MLAR-BBAR had different prescriptions for different glass materials but showed nearly identical responses in the vendor-supplied spectral data. Hence, we deemed it reasonable to use the N-th root approach to assessing the MLAR-BBAR contribution to the throughput deficit on a per-surface transmission basis. The same applies to the rARSS treatment.

The result seems to suggest that the MLAR-BBAR, for some reason, incurred 0.5% or so more loss per surface than their witness samples suggested. Given the large number of air-glass interfaces in the AWACS unit, such a small loss can build up to a considerable throughput loss. The rARSS largely shows a similar spectral response to that of its witness samples except for the wavy features in certain wavelength regions, which we suspect are artifacts from the above reduction procedure. The main take-away of this analysis is that while it is not ideal to see the sub-optimal performance of the MLAR-BBAR, the rARSS treatment seems to perform as expected at a system level and could be useful in providing AR capability, along with the existing MLAR, to a complex optical system for astronomy like the AWACS units.

In addition to the throughput performance, we evaluated how the rARSS contributed to the system-level imaging performance. For this, each unit was tested as a standalone relay without the telescope in terms of image quality. As shown in the left panel of Fig. 8, each unit was integrated to a complementary metal oxide semiconductor (CMOS) sensor from Teledyne (Kinetix $3K \times 3K - 6.5$ μm). The CMOS sensor has 20 mm × 20 mm detector area, sufficiently large to cover the unit field of view (FOV). A well-characterized reticle target is placed at the front object plane of the unit, illuminated by a bright and diffuse broadband light source (LDLS from Hamamatsu). The target contains nine 50 μm diameter spots in a cross-hair pattern with larger disks and rectangles around to indicate direction and orientation. The unit relays the illuminated target image onto the CMOS detector (Fig. 8, right panel.) The reticle target pattern is smaller than the detector area. To sample the image quality across the entire FOV including those corners, the reticle was placed on a translation stage and moved across the FOV. The size and
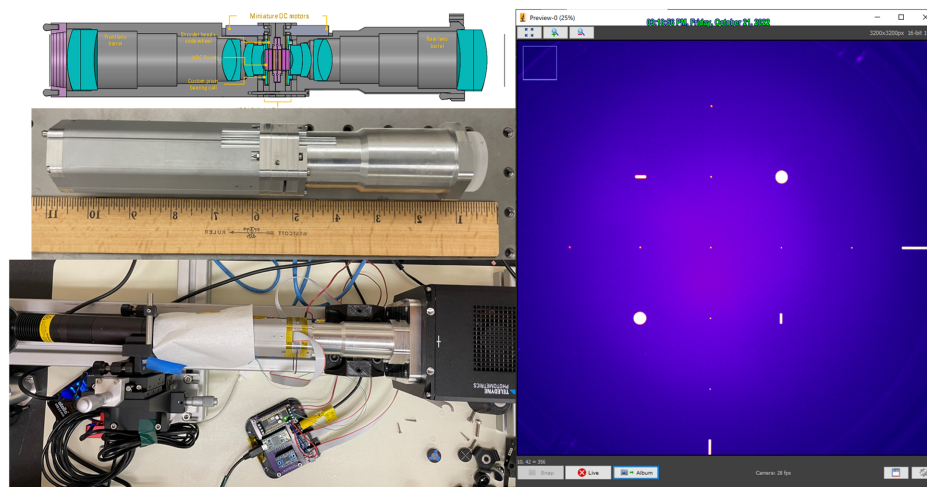

Fig. 8 (Top-left) The optomechanical design and actual build of an AWACS unit. (Bottom-left) AWACS U1 under image quality evaluation. (Right) A well-defined target pattern is illuminated by a broadband light source and then imaged through U1 onto a CMOS detector. The image spots of the target pattern are analyzed to determine the size of the point spread function across the image plane to determine the unit's image quality.
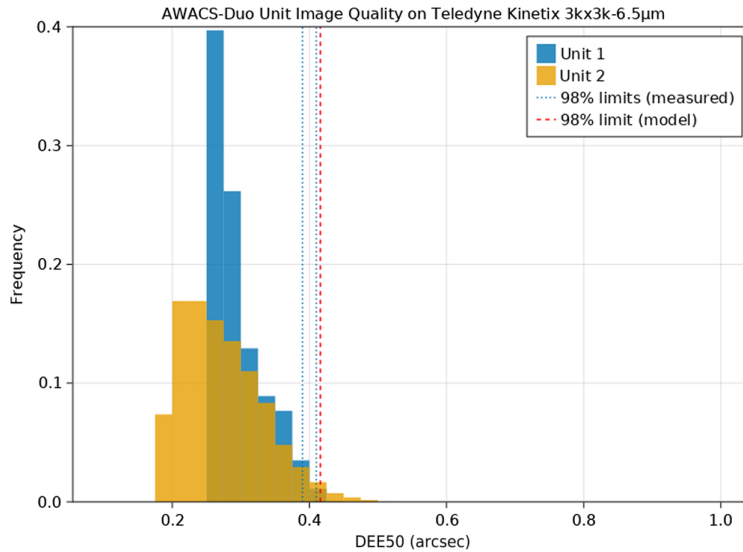
Fig. 9 AWACS unit image quality distribution over the unit's FOV against the model prediction. Image quality is given in diameter of 50% enclosed energy.

sharpness of the relayed spots were used to determine the image quality of each unit. For this evaluation, the ADC prisms and cylinder pairs were all adjusted to their respective neutral positions where they do not impart additional spectral dispersion or astigmatism to the unit's transmitted wavefront. In so doing, we have aligned these neutral axes to the required orientations for on-sky subsystem functionality. The image quality distribution of each unit across the FOV captured on the CMOS sensor is shown in Fig. 9. The image quality is given in terms of the diameter of 50% point spread function enclosed energy measured across the field. The median DEE50 is 0.27 arcsec for U1 and 0.24 arcsec for U2. These values compare well to the model median prediction of 0.26 arcsec. The DEE50 across 98% of the unit's FOV is found to be less than 0.40 arcsec, comparing favorably to the model 0.42 arcsec prediction at the same limit. This standalone image quality test strongly suggests that both units' imaging performance meets expectations, but more importantly, as indicated by the wavefront measurement discussed earlier, the rARSS seems to have no considerable impact on the system's imaging performance.

In March 2023, we were able to test the AWACS-Duo system on-sky on the 2.7 m HJST at the McDonald Observatory in Fort Davis, Texas, United States. We were only able to compare the relative throughput between two units by measuring the total integrated flux of the same star [HD73709 at (RA,DEC) coordinate of (08 40 22.015, +19 40 11.87)]. We fitted a 2D Moffat function to the stellar PSFs to estimate the total flux and found only 1.3% relative difference between the two units. The on-sky imaging performance was also consistent between the two units. With respect to the native telescope focus, the units' DEE50 was <2% different. This confirms the system-level throughput and imaging performance consistency with the lab measurements, while we attribute these very small relative differences to a photometry error.

5 Conclusions

Randomly distributed anti-reflective nanostructures were fabricated on FS cylindrical lenses and freeform optical elements, using a plasma-assisted reactive-ion etching technique. We examined the transmission-enhancing impact of the random nanostructures on the surfaces before their use as components of an arrayed wide-field astronomical corrector unit.

The total spectral transmission of all component sets tested achieved values over 98%, over a wavelength range of 400 to 500 nm across the entire visible spectrum, without localized extrema. Component transmission over 99% was measured across a narrower 40 to 100 nm band, centered around wavelengths of 470 nm for the cylindrical lenses and 540 nm for the FF. The difference in spectral transmission between the rARSS-enhanced lenses and the FF is attributed to fabrication

effects due to the optical component's physical dimensions. The FF were three times larger in aperture diameter and thickness, compared to the lenses. During the rARSS fabrication, the components sit on a platen and are exposed to the RIE plasma driven by a high-power RF-signal. The etch chamber configuration is identical to a large parallel-plate capacitor, with the signal field driven between the platen and the cover plate. The substrate surface etch rate depends on the separation between the exposed surface and the boundary of the plasma. Thicker substrates have smaller separations, resulting in different etch characteristics from thinner substrates. The substrate diameter affects etch uniformity across the surfaces. Larger diameter surfaces result in the generation of more etch by-products that slow the process and have more center-to-edge uniformity variance. Overall, the results shown in Fig. 2 are very consistent and meet the spectral transmission requirements of the system unit.

We also found that the cylindrical wavefronts emerging from the lenses were not adversely affected by the rARSS fabrication process, nor did the rARSS perturb the performance of the lenses to a degree of concern. The emerging wavefronts have post-process larger negative values for Z_5 and smaller positive values for Z_6. This observation indicates that the PCX/PCV surfaces are etched somewhat differently from center to edge. We measured a Zernike-defocus change from $\lambda/10$ to $\lambda/8$ (at 633 nm), related to the respective convexity or concavity of the lenses, and the Zernike-astigmatism post-process wavefront performance had the same deviation values.

To detect any off-axis light scatter, we measured the bidirectional scatter distribution function of selected locations on the freeform element, after applying rARSS. The testing laser-system-signature spot diameter was not affected at all by the presence of the transmission-enhanced FF, maintaining a $1/e^2$ full-angle divergence of 0.15 deg and an unperturbed radiance distribution over five-orders of magnitude within the entire axially projected full-angle of 10 deg. This is an indication of an absence of scatter to a radiance level equivalent to $1/e^{11}$.

The enhanced elements were placed in an arrayed wide-field astronomical camera system unit assembly, and comparative field tests were performed in the laboratory and with the HJST at the McDonald Observatory. The end-to-end spectral and imaging tests clearly indicated that two units exhibited nearly identical imaging and throughput characteristics, that the applied rARSS showed a transmission profile consistent with the expectation based on its sample measurements, particularly near the short wavelengths, and that the system demonstrated no visible degradation in its PSFs across the designed FOV. All of these were confirmed by the on-sky measurement at the HJST.

To our knowledge, this is the first report of functional BBAR-FF elements with rARSS, as well as, this is the only report at present that compares the function of rARSS-enhanced components in a complete optical system.

Disclosures

Code and Data Availability

There are no associated codes for this work. Some of the data products used in the paper are subject to the NSF data management plan for archival purposes within the Texas Data Repository (TDR) at the University of Texas - Austin from which the data will be accessed. The exact types of data to be archived at the TDR will be determined toward the end of the NSF program in 2024 and we expect the access to those data products be available starting in 2025. There are other data types that affect the accuracy and quality of the final measurements used in the paper. These are heavily influenced by the exact measurement setup, specific instruments and tuning characteristics, and environmental conditions many of which have been developed outside the scope of the work described in the paper and fall in the proprietary category of the institutions involved. We anticipate that the access to such data may be requested on a case-by-case basis through communication with the authors involved.

Acknowledgments

References

1. H. Shimomura et al., "Layer-by-layer-assembled high-performance broadband antireflection coatings," *ACS Appl. Mater. Interfaces* **2**(3), 813–820 (2010).
2. P. M. Kaminski, G. Womack, and J. M. Walls, "Broadband anti-reflection coatings for thin film photovoltaics," in *IEEE 40th Photovoltaic Specialist Conf. (PVSC)*, pp. 2778–2783 (2014).
3. K.-H. Kim and Q.-H. Park, "Perfect anti-reflection from first principles," *Sci. Rep.* **3**(1), 1–5 (2013).
4. K. Wei-Jin et al., "Graded index broadband antireflection coating prepared by glancing angle deposition for a high-power laser system," *Chin. Phys. B* **19**(4), 044210 (2010).
5. M. Chen et al., "Design of optical path for wide-angle gradient-index antireflection coatings," *Appl. Opt.* **46**(26), 6533–6538 (2007).
6. C. Martinet et al., "Deposition of SiO_2 and TiO_2 thin films by plasma enhanced chemical vapor deposition for antireflection coating," *J. Non-Cryst. Solids* **216**, 77–82 (1997).
7. H. Hattori, "Anti-reflection surface with particle coating deposited by electrostatic attraction," *Adv. Mater.* **13**(1), 51–54 (2001).
8. S.-H. Jeong et al., "Characterization of SiO_2 and TiO_2 films prepared using RF magnetron sputtering and their application to anti-reflection coating," *Vacuum* **76**(4), 507–515 (2004).
9. D. Vandormael et al., "Anti- reflective sub-wavelength patterning of IR optics," *Proc. SPIE* **6395**, 63950L (2006).
10. D. S. Hobbs, B. D. MacLeod, and J. R. Riccobono, "Update on the development of high performance anti-reflecting surface relief micro-structures," *Proc. SPIE* **6545**, 242–255 (2007).
11. R. Joshi, G. J. Gbur, and M. K. Poutous, "Fabrication of broadband anti- reflective surface on fused silica from visible to SWIR spectral band," in *Novel Opt. Mater. and Appl.*, Optica Publishing Group, p. NoW2D–3 (2019).
12. L. E. Busse et al., "Review of antireflective surface structures on laser optics and windows," *Appl. Opt.* **54**(31), F303–F310 (2015).
13. L. E. Busse et al., "Harsh environment tests of random antireflective surface structures on optics," in *Conf. Lasers and Electro-Opt. (CLEO)*, IEEE, pp. 1–2 (2017).
14. L. E. Busse et al., "Anti-reflective surface structures for spinel ceramics and fused silica windows, lenses and optical fibers," *Opt. Mater. Express* **4**(12), 2504–2515 (2014).
15. C. Taylor et al., "Optical performance of random anti-reflection structures on curved surfaces," *Proc. SPIE* **9359**, 935916 (2015).
16. C. D. Taylor et al., "Angle-of- incidence performance of random anti-reflection structures on curved surfaces," *Appl. Opt.* **55**(9), 2203–2213 (2016).
17. K. Pfeiffer et al., "Antireflection coatings for strongly curved glass lenses by atomic layer deposition," *Coatings* **7**(8), 118 (2017).
18. C. Pacholski et al., "Antireflective subwavelength structures on microlens arrays—comparison of various manufacturing techniques," *Appl. Opt.* **51**(1), 8–14 (2012).
19. H. Lee et al., "Arrayed wide-angle camera system for the Extremely Large Telescopes," *Proc. SPIE* **10702**, 107021Z (2018).
20. H. Lee et al., "Arrayed wide-angle camera system for wide field imaging and spectroscopy on ELTs: proof-of-concept on-sky test results on McDonald Observatory 2.7 m telescope," *Proc. SPIE* **11445**, 114453W (2020).
21. H. Lee and M. K. Poutous, "Arrayed wide-field astronomical camera system for spectroscopic surveys on Extremely Large Telescopes: system architecture, proof-of- concept, and enabling technologies," *J. Astron. Telesc. Instrum. Syst.* **7**(3), 035007 (2021).
22. H. Lee et al., "Integration/test of dual unit arrayed wide-angle camera system and its evaluation in the context of extremely large telescopes," *Proc. SPIE* **12184**, 121848E (2022).
23. U. Subash, H. Lee, and M. K. Poutous, "UV to IR high-efficiency antireflective surface modification of freeform and cylindrical lenses for space platform optical instrumentation," *Proc. SPIE* **12676**, 126760H (2023).
24. A. P. Eckart et al., "Control of spectral transmission enhancement properties of random anti-reflecting surface structures fabricated using gold masking," *Proc. SPIE* **10115**, 101150B (2017).
25. D. Malacara, *Optical Shop Testing*, Vol. **59**, John Wiley & Sons (2007).
26. V. Lakshminarayanan and A. Fleck, "Zernike polynomials: a guide," *J. Mod. Opt.* **58**(7), 545–561 (2011).

Uma Subash is a doctoral candidate in the Department of Physics and Optical Science at the University of North Carolina - Charlotte. She has a master's degree in optical engineering, and she received her BSMS degree in physics from IISER Thiruvananthapuram in 2019.

Hanshin Lee is a senior research scientist at the McDonald Observatory at the University of Texas–Austin. He graduated from the University of Oxford and has been continuing his PhD specialty in astronomical instrumentation with emphasis on design, construction, and commissioning of large-scale spectroscopic instruments and telescope systems and software and hardware technique development for device- and system-level metrology and performance evaluation in astronomy applications.

Menelaos K. Poutous is an associate professor of physics and optical science at UNC Charlotte. He previously held a principal development engineer's position with Digital Optics Corporation and before that he was a lecturer of physics at Emory University. He received his doctorate in 1996 from the School of Physics at the Georgia Institute of Technology. His research interests are in spectroscopy, diffractive nano- and micro-optical elements, photolithographic microfabrication, and artificial optical surfaces.